Word count: 5851, Revision 1

Experimental determination of carbon diffusion in liquid iron at high pressure

Anna M. Rebaza[1,2,3], Esther S. Posner[1*], Marcel Thielmann[1], David C. Rubie[1], Gerd Steinle-Neumann[1]

[1] Bayerisches Geoinstitut, Universität Bayreuth, 95440 Bayreuth, Germany

[2] Department of Geosciences, University of Rhode Island, Kingston, RI 02881, USA

[3] Department of Geosciences, University of Arizona, Tucson, AZ 85721, USA

[*]Corresponding author. E-mail: esther.posner@uni-bayreuth.de Tel.: +49 (0) 921 55 3735, Fax: +49 (0) 921 55 3769

ABSTRACT

The transport properties of liquid iron alloys at high pressure (P) and temperature (T) are essential for understanding the formation, composition, and evolution of planetary cores. Light alloying elements (e.g., Si, O, S, C, N, H) in liquid iron are particularly relevant due to the density deficit of Earth's core, yet high P-T experimental diffusion studies involving such alloys remain scarce with large uncertainties on the P and T dependence required for extrapolation to core conditions. In this study, we measured the chemical diffusion rates of carbon in liquid iron over a P-T range of 3–15 GPa and 1700–2450 K using a multi-anvil apparatus. Diffusion couples consisting of pure Fe and Fe-2.5wt.%C cylinders were placed end-to-end in an MgO capsule in a vertical orientation. Carbon concentration profiles were measured by electron microprobe and modeled numerically to correct for non-isothermal diffusion that occurred prior to reaching the peak temperature. Carbon diffusion coefficients range from 6×10^{-9} $m^2 \cdot s^{-1}$ to 2×10^{-8} $m^2 \cdot s^{-1}$, with global Arrhenian fit parameters $D_0 = 1.4 \pm 0.5 \times 10^{-7}$ $m^2 \cdot s^{-1}$, $\Delta E = 43 \pm 6$ $kJ \cdot mol^{-1}$, and $\Delta V = -0.06 \pm 0.19$ $cm^3 \cdot mol^{-1}$. A negligible P effect is consistent with previous studies of oxygen diffusion in liquid iron and high-T

calculations, but differs from larger ΔV values previously reported from carbon self-diffusion experiments for liquid Fe_3C and simulations for an Fe–Ni–C alloy. Carbon diffusion coefficients determined here are approximately three times faster than those reported from Fe–Ni–C liquid simulations, which highlights the potential significance of compositional effects on mass transport properties of liquid iron alloys and the need for expanding the *P*-*T* experimental diffusion dataset currently available in the literature to more complex and geologically relevant compositions.

Keywords: carbon diffusion; core formation; outer core; liquid iron alloys; interstitial alloys

INTRODUCTION

The distribution of carbon in reservoirs of the Earth's interior plays a critical role in a range of geological processes, including climate, habitability, and potentially the geodynamo (e.g., Hazen and Schiffries, 2013). Carbon is a siderophile element (e.g., Dasgupta et al., 2013; Li et al., 2015, 2016; Fischer et al., 2020), which implies that the majority (80%–90%) of the Earth's carbon budget is expected to have partitioned into the core during planetary differentiation owing to metal-silicate segregation. The extent of chemical equilibration between metal and silicate during core formation is largely controlled by diffusion kinetics of alloying elements in iron-rich liquid metal under relevant magma ocean pressure (*P*) and temperature (*T*) conditions (e.g., Rubie et al., 2003).

Most diffusion studies in liquid iron and its alloys have reported weak *P*-*T* dependences with small Arrhenian activation parameters (e.g., Poirier, 1988; Ichikawa and Tsuchiya, 2015; Umemoto and Hirose, 2015; Posner et al., 2017a, 2017b) according to

$$D_i(P,T) = D_0 \exp -\left(\frac{\Delta E + P\cdot\Delta V}{R\cdot T}\right), \quad (1)$$

where D_i is the diffusion coefficient of element *i*, D_0, ΔE, and ΔV are the pre-exponential diffusion coefficient, activation energy, and activation volume, respectively, and *R* is the gas

constant. For isobaric fits, the numerator in the exponent is replaced by an enthalpy ΔH^* (e.g., Ni et al., 2015) and the pre-exponential factor is labeled as D_0^* in these cases. Carbon is incorporated interstitially into both solid (e.g., Goldschmidt, 1967) and liquid iron (e.g., Sobolev and Mirzoev, 2013; Ohmura et al., 2020) and is therefore expected to show relatively similar diffusion behavior to other interstitial elements (e.g., O and N) as predicted by density-functional molecular dynamics (DFT-MD) simulations (e.g., Posner and Steinle-Neumann, 2019).

High *P*-*T* experiments involving oxygen revealed a negligible *P* effect on diffusion rates in liquid iron between 3 and 18 GPa (Posner et al., 2017b). However, a high *P*-*T* experimental study of carbon self-diffusion in liquid Fe_3C (Dobson and Wiedenbeck, 2002) and recent isothermal (T = 1675 K) computations for liquid $Fe_{0.73}Ni_{0.07}C_{0.20}$ (Wang et al., 2019) reported ΔV values of carbon self-diffusion that are substantially larger (ΔV ~ 1.2 $cm^3 \cdot mol^{-1}$) than values reported for oxygen ($\Delta V = 0.1 \pm 0.1$ $cm^3 \cdot mol^{-1}$; Posner et al., 2017b) and hydrogen (ΔV ~ 0.2 $cm^3 \cdot mol^{-1}$; Umemoto and Hirose, 2015), and also for substitutionally incorporated silicon ($\Delta V = 0.41 \pm 0.06$ $cm^3 \cdot mol^{-1}$; Posner et al., 2017a) and chromium ($\Delta V = 0.34 \pm 0.11$ $cm^3 \cdot mol^{-1}$; Posner et al., 2017a).

Although Dobson and Wiedenbeck (2002) and Wang et al. (2019) reported similarly large ΔV values, their absolute D_C values differ by nearly a factor of three. Combined with large errors on the activation parameters reported by Dobson and Wiedenbeck (2002), uncertainties on the carbon diffusion coefficient in liquid iron alloys at high *P*-*T* relevant to metal-silicate equilibration conditions in a deep magma ocean and the Earth's outer core span several orders of magnitude.

To address this problem, we performed carbon chemical diffusion experiments on liquid iron over a wider range of *P* (3, 8, 15 GPa) and *T* (1700–2450 K) using Fe–Fe-2.5wt.%C diffusion couples and compare our results with those of previous experimental and

computational studies. Our results show a negligible *P* effect on carbon chemical diffusion below 15 GPa, similar to the behavior of oxygen in liquid iron over the same *P* range. We use the refined diffusion parameters to estimate D_C at *P-T* conditions relevant to metal-silicate equilibration in a deep magma ocean and Earth's outer core.

MATERIALS AND METHODS

Starting material

Diffusion couples consisted of 1.2-mm diameter cylinders of iron and iron alloy, each with a length of 1.0 mm (Fig. 1). Iron cylinders of 99.98% purity were machined with ends polished to a 0.25-μm finish. The alloy (Fe-2.5wt.%C) was prepared from a mixture of fine-grained metallic powders of Fe and graphite (each with purity of 99.9%). Powders of this mixture were packed tightly into an MgO capsule, which was then loaded into a Mo-foil capsule, and sintered into solid rods in a piston-cylinder apparatus at 1.5 GPa and 1323 K for 6 h using a talc-pyrex pressure assembly and a graphite furnace (Fig. S1). Sintered rods were removed, cut, polished on the ends to a 0.25-μm finish, and checked for chemical homogeneity by electron microprobe (Table S1).

Experimental procedure

Chemical diffusion experiments were performed in 1200 and 5000 t multi-anvil presses at the Bayerisches Geoinstitut using MgO(+5 wt.% Cr_2O_3) octahedra with 18-mm edge lengths as the pressure medium (Fig. 1). Eight 32-mm cubes of tungsten carbide with 11-mm corner truncations were used to generate *P*. The assembly design is identical to that used in previous diffusion studies in our laboratory (Posner et al., 2017a, 2017b). All diffusion couples were contained vertically within an MgO capsule (Fig. 1), with the less-dense alloy on top to maintain gravitational stability (Posner et al., 2017a). Stepped $LaCrO_3$

heaters were used in order to minimize the T gradient along the sample (Rubie, 1999). Temperature was monitored using a $W_{97}Re_3$-$W_{75}Re_{25}$ thermocouple with the junction placed above the MgO capsule lid, 0.75 mm from the top of the metallic diffusion couple.

Experiments were performed at 3, 8, and 15 GPa in order to reproduce the experimental conditions (8 and 15 GPa) studied by Dobson and Wiedenbeck (2002). We added experiments at P = 3 GPa to better constrain the effect of P on carbon diffusion in liquid iron. Samples were slowly compressed to the desired multi-anvil press load and heated using a proportional-integral-derivative controller with output temperature values recorded every 0.1 s. To minimize diffusion prior to reaching the peak anneal temperature (T_p), all experiments were heated from room temperature to 1073 K in 480 s, maintained at this temperature for 60 s, rapidly heated with a constant ramp rate (dT/dt) of 20–100 $K \cdot s^{-1}$ to T_p, maintained at T_p for time t_p, and then quenched by shutting off the electrical power (Fig. S2). Initial quench rates were in excess of 400 $K \cdot s^{-1}$. Temperatures and associated errors listed in Table 1 are the average and standard deviation values of T_p measured during the post-ramping stage, respectively. Rapid equilibration (due to fast diffusion) of mm-sized samples limited t_p to 9–39 s (Table 1).

Analytical procedure

Recovered samples were cut and polished parallel to the cylindrical sample axis (Fig. 2) immediately prior to analysis by electron microprobe (EPMA). A thin line of silver paint was used to ensure conductivity between the metallic samples and sample holder. Spot analysis measurements across the entire sample were made along a line perpendicular to the diffusion interface using a JEOL-JXA-8200 EPMA. Carbon-rich melts quenched into coexisting carbon-rich dendritic crystals (<20 μm) surrounded by a carbon-poor matrix (Fig. 2b). As a consequence, measurements using a small beam diameter (10 μm) yielded

significant scatter on the initially carbon-bearing side of the diffusion couple. To effectively analyze both matrix and crystals, we used a defocused beam with an effective diameter of ~70 μm, which substantially reduces the data scatter, similar to our prior work on oxygen diffusion in liquid iron (Posner et al., 2017b). The probe current and accelerating voltage were 15 nA and 15 kV, respectively. Standards used were pure Fe and Fe_3C metals, the latter was synthesized at BGI (Blanchard et al., 2019). Counting times were 10 s on the peak and 5 s on the background. The analytical error on carbon analyses is in the range between 5% and 10%. Line scans were between 1570 μm and 1810 μm in length and the spacing between analyzed spots was 60 μm. At least two parallel scans were made on each sample to assure reproducibility and to rule out mechanical (convective) mixing.

Data fitting

The problem of non-isothermal diffusion annealing for experimental samples with large diffusion coefficients, such as liquid metals, is addressed in detail in Posner et al. (2017a). In low-viscosity molten materials, diffusion occurs not only at T_p but also during the heating stage between the melting temperature (T_m) and T_p. Rapid heating rates and a long duration t_p are required to minimize the contribution of diffusion occurring between T_m and T_p. A full discussion of the effects of dT/dt, magnitude of $T_p - T_m$, and t_p is provided in the supplemental material of Posner et al. (2018) and is not repeated here. As outlined in our previous studies, we correct for non-isothermal annealing using (i) variable heating rates (20–100 $K \cdot s^{-1}$) and different T_p values and (ii) a numerical approach to retrieve diffusion parameters from the simultaneous fitting of several profiles obtained at the same P. The numerical scheme is the same as that used in previous high-P experimental diffusion studies involving liquid metals (Posner et al., 2017a, 2017b) and peridotite melt (Posner et al., 2018).

Concentrations at both ends of the sample changed during the experiments due to diffusion, which implies that the sample cannot be considered to have been a semi-infinite reservoir. To treat the sample as a finite reservoir, we fitted the concentration profiles using Crank-Nicolson finite difference modeling with boundary conditions of zero concentration gradient at both sample ends. The "amoeba" algorithm (Press et al., 2002), which performs multidimensional minimalization using the downhill simplex method, was used for least-square regressions.

The interface location (x_0) was first determined for each concentration profile by refining x_0 together with an "effective" diffusion coefficient. The latter was subsequently discarded as it does not account for non-isothermal diffusion. Using the determined interface locations, we simultaneously refined isobaric D_0^* and ΔH^* values, i.e., ignoring the P dependence in Eq. (1), for all profiles obtained at a single P (Table 1). The simulation began at T_m and incorporated the experimental dT/dt, T_p, t_p, and x_0 values for each concentration profile and a time step of 0.1 s. We minimized the squared sum of weighted residuals χ^2 and report the reduced values, $\chi^2_{red} = \chi^2/u$, where u is the number of degrees of freedom determined as $u = N - n - 1$ with N the number of observations and n the number of fitted parameters (here $n = 2$: D_0^* and ΔH^*).

In previous studies, we used T_m as that of pure iron (Posner et al. 2017a, 2017b), which is too high for Fe-2.5wt.%C because the liquidus T in the Fe–C phase diagram rapidly decreases with carbon content (Okamoto, 1992). Although T_m of pure iron at 1 bar is 1811 K (Swatzendruber, 1982), our samples show evidence of melting at 1700 K and 3 GPa (Fig. 3a) indicated by carbon dissolution into the initially pure iron cylinder across the carbon-rich melting front. To address this issue, we varied T_m between 1423 K – the eutectic T in the Fe-Fe_3C phase diagram at 1 bar – and 1700 K in the model, and found refined parameters to be

insensitive to this variation. We therefore settled on a conservative T_m = 1423 K at each P to account for the diffusion that occurred during heating.

The parameters of Eq. (1), D_0, ΔE, and ΔV, were determined by equally weighing the results obtained at the three different P, irrespective of the number of measurements at each P (Table 2).

RESULTS AND DISCUSSION

Carbon concentration profiles from two experiments each at 3 and 15 GPa are shown in Fig. 3 with a similar target T_p and dT/dt values, but varying t_p. With increasing t_p, concentration profiles flatten, as they do with increasing T_p (Fig. 3). Isobaric best fits (N = 5 at 3 and 15 GPa, N = 3 at 8 GPa) are compared to the measured profiles in Figs. 3 and 4. The diffusivity of carbon in liquid iron varies between 6×10^{-9} m^2·s^{-1} and 2×10^{-8} m^2·s^{-1} over the P-T range investigated here. This is essentially identical to the diffusivities of oxygen within the associated errors (Posner et al., 2017b), representing another interstitially incorporated alloying element (Posner and Steinle-Neumann, 2019), and approximately 2–3 times faster than substitutionally incorporated Si and Cr (Posner et al., 2017a). This is likely related to different diffusion mechanisms for C and O versus Si and Cr, which depend on their relative atomic size compared to iron, similar to vacancy-mediated exchange along different sites within crystalline material (e.g., anion vs. cation diffusion with different atomic jump frequencies), as extensively discussed in Posner and Steinle-Neumann (2019).

The refined isobaric chemical diffusion parameters (D_0^* and ΔH^*) determined at each P are listed in Table 1 and Arrhenian fits are shown in Fig. 5 over the experimental T range at each P investigated. Activation enthalpies ΔH^* are small (<70 kJ·mol^{-1}) and decrease slightly with P from $\Delta H^* = 59 \pm 5$ kJ·mol^{-1} at 3 GPa to 44 ± 4 kJ·mol^{-1} at 8 GPa to 31 ± 6 kJ·mol^{-1} at 15 GPa (Table 1). These values are consistent with previously reported ΔE values for

carbon self-diffusion in liquid Fe_3C (37 ± 70 kJ·mol^{-1}; Dobson and Wiedenbeck, 2002) but with significantly reduced errors, as well as values for the diffusion of oxygen (ΔE = 62 ± 6 kJ·mol^{-1}; Posner et al., 2017b, ΔE = 55–83 kJ·mol^{-1}; Ichikawa and Tsuchiya, 2015), hydrogen (ΔE = 44–77 kJ·mol^{-1}; Umemoto and Hirose, 2015), silicon (ΔE = 39 ± 4 kJ·mol^{-1}; Posner et al., 2017a), and chromium (ΔE = 42 ± 7 kJ·mol^{-1}; Posner et al., 2017a) in liquid iron.

Our data at 15 GPa are in excellent agreement with experimental carbon self-diffusion values reported by Dobson and Wiedenbeck (2002) and extrapolate well to results from the DFT-MD simulations by Posner and Steinle-Neumann (2019) at higher *T*, while our data at 8 GPa show that carbon chemical diffusion is slower by a factor of ~2 compared to self-diffusion in the experiments by Dobson and Wiedenbeck (2002) (Fig. 5), and also slightly slower than the DFT-MD self-diffusion results by Posner and Steinle-Neumann (2019) for a dilute C concentration ($Fe_{0.96}C_{0.04}$). Our diffusion data at 3 GPa agree with the low-*P* self-diffusion results of Wang et al. (2019) and again extrapolate well to the results by Posner and Steinle-Neumann (2019), but a significant discrepancy appears at higher *P* between our data and the simulations of Wang et al. (2019).

A negligible *P* dependence between 3 and 15 GPa according to our data (ΔV = −0.06 ± 0.19 cm^3·mol^{-1}; Table 2) is in good agreement with previous experiments on chemical diffusion of oxygen (ΔV = 0.1 ± 0.1 cm^3·mol^{-1}; Posner et al., 2017b) (Fig. 5) and high-*T* simulations of carbon self-diffusion in liquid $Fe_{0.96}C_{0.04}$ (Posner and Steinle-Neumann, 2019). However, this finding is in conflict with the larger *P* dependence reported for carbon self-diffusion in liquid Fe_3C (ΔV = 1.3 ± 0.5 cm^3·mol^{-1}; Dobson and Wiedenbeck, 2002) from experiments at 8 and 15 GPa and the isothermal simulations by Wang et al. (2019) on liquid $Fe_{0.73}Ni_{0.07}C_{0.20}$ who determined ΔV = 1.2 ± 0.3 cm^3·mol^{-1} for $P \lesssim 5$ GPa and ΔV = 0.61 ± 0.09 cm^3·mol^{-1} for $P \gtrsim 5$ GPa. A changing value of ΔV with *P* is plausible on two grounds:

(i) Our diffusion data at 3 GPa are slower by a factor of ~1.5 compared to data at 1 bar (Yang et al., 1956), suggesting a larger and positive ΔV at low P; (ii) a change in ΔV is likely attributed to a change of carbon coordination from ~6 to ~8 upon compression (Wang et al., 2019; Posner and Steinle-Neumann, 2019). However, DFT-MD results for liquid $Fe_{0.96}O_{0.04}$ reported the opposite behavior: a slight increase of ΔV for oxygen diffusion with P upon the completion of Fe and O coordination changes (Posner et al., 2017c).

In terms of the experimental results, it is important to note that the ΔV differences between our study and Dobson and Wiedenbeck (2002) may be due to a combination of both experimental design and modeling protocol: (i) carbon concentration (~2.5 wt.% here vs. ~7 wt.% in Dobson and Wiedenbeck, 2002); (ii) measurements of chemical diffusion using a compositional gradient in this study vs. self-diffusion using a thin-film ^{13}C isotopic gradient in Dobson and Wiedenbeck (2002); (iii) different capsule material (MgO here vs. Al_2O_3 fitted in a Zr-foil capsule in Dobson and Wiedenbeck (2002)), which may have led to slight differences in oxygen fugacity; and (iv) model fitting, first at each individual P and then over the global P range using the isobaric results (here) vs. global modeling only in Dobson and Wiedenbeck (2002). Of these possibilities, we believe that carbon concentration likely has the strongest influence. Increasing carbon content leads to a decrease in density of solid and liquid iron alloys (e.g., Terasaki et al., 2010), which reflects changes in the extent of atomic packing of both iron and carbon. Pure liquid iron has been shown to transform from a bcc-like structure to a close-packed-like structure near the γ-δ-liquid triple point (e.g., Sanloup et al., 2000), which changes the relative size of tetrahedral and octahedral voids. This has been used to explain a change in diffusion mechanism and negligible ΔV of interstitial oxygen in dilute $Fe_{0.96}O_{0.04}$ (Posner et al., 2017c) and is also likely applicable for carbon in low-C alloys such as those used here. In contrast, Fe_3C is already close-packed at ambient P (e.g., Wood et

al., 2004), thus a similar carbon diffusion mechanism change likely does not occur in liquid Fe_3C.

It is important to reiterate that although Dobson and Wiedenbeck (2002) and Wang et al. (2019) reported larger ΔV values than those determined here and in previous studies of diffusion in binary Si-, O-, and H-bearing liquid iron alloys, the absolute values of their D_C differ by nearly a factor of three (Fig. 5). Carbon diffusion coefficients reported by Wang et al. (2019) are also a few times smaller than D_C computed by Posner and Steinle-Neumann (2019) when applying ΔE = 30–60 kJ·mol^{-1} to the former in order to extrapolate with T. A possible explanation for slower carbon diffusion in the DFT-MD simulations by Wang et al. (2019) may be related to the presence of Ni, which has been shown to reduce the mobility of interstitial clusters in solid Fe-Ni alloys due to repulsive interactions between Ni and interstitial atoms (Osetsky et al., 2015; Anento et al., 2017). A similar process is likely relevant in the liquid as its short-range order mimics that of the solid-state structure near T_m (e.g., Campbell, 2008). Furthermore, average Fe-Ni interatomic distances have been shown to be larger than Fe-Fe distances in binary liquid $Fe_{0.96}Ni_{0.04}$ by 2%–4% at low P (Posner and Steinle-Neumann, 2019), which may reduce (i.e., crowd) interstitial diffusion pathways preferred by carbon and therefore lead to slower diffusion rates. However, the role of Ni in increasing ΔV of carbon diffusion (and possibly other interstitial elements), compared to the small ΔV obtained in the present study in the Fe–C binary, remains quantitatively unclear and should be examined experimentally over similar P-T conditions.

IMPLICATIONS

In the inset of Fig. 5, we compare carbon diffusion coefficients extrapolated to conditions pertaining to a deep magma ocean (54 GPa, 4100 K; Rubie et al., 2015) using (i) the global Arrhenian parameters determined in this study (Table 2) and (ii) by Dobson and

Wiedenbeck (2002), (iii) a ΔE range of 30–60 kJ mol^{-1} to extrapolate D_C reported by Wang et al. (2019) to high T, and (iv) interpolating between P-T points of Posner and Steinle-Neumann (2019). Under these conditions, the error bars on the extrapolated values are notably smaller when using the parameters determined in the present study (±0.4 log units) than the extrapolation of the data by Dobson and Wiedenbeck (2002) (±1.6 log units). Values of diffusivity from the four studies overlap tightly within their uncertainties in the range of D = 2–3 × 10^{-8} m^2·s^{-1}, which is identical within error to oxygen diffusion and ~2.5 times faster than silicon. If we assume that the degree of chemical exchange between metallic and silicate melts is largely controlled by diffusive transport in liquid iron, carbon and oxygen would reach equilibrium values approximately 60% faster than silicon with a ~1.6 times longer effective diffusion distance. Owing to the similarity of carbon and oxygen diffusivities and Arrhenian parameters (Table 2), our findings further support previous conclusions (e.g., Posner et al., 2017b) that the chemical equilibration of these elements in descending metallic droplets within a magma ocean would be limited to droplet radii of less than a few tens of centimeters.

Extrapolation of our results to outer core conditions yields D_C ~ 5 × 10^{-8} m^2·s^{-1} at the core-mantle boundary (135 GPa, 4000 K) and ~9 × 10^{-8} m^2·s^{-1} at the inner-core boundary (329 GPa, 6000 K); these values may be overestimates, however, owing to a potential mobility reduction resulting from compositional effects related to the presence of Ni (Wang et al., 2019) and/or an increase of ΔV at higher P, similar to that reported for the diffusion of oxygen (Posner et al., 2017c) and other alloying elements that are incorporated interstitially (Posner and Steinle-Neumann, 2019). Because experimental diffusion data are presently limited to binary liquid iron alloys, our discussion highlights the need for further studies involving multi-component Ni-bearing iron alloy liquids (e.g., Fe–Ni–C, Fe–Ni–S–C) to

297 constrain compositional effects on the mass transport properties of Fe–Ni–light element
298 liquids to more appropriately represent conditions relevant to planetary cores.
299

300 **ACKNOWLEDGMENTS**

301 We thank Rafael Njul, Alexander Rother, Heinz Fischer, and Stefan Übelhack for
302 experimental sample and assembly preparation, Sumith Abeykoon and Svyatoslav Shcheka
303 for assistance with the multi-anvil experiments, Florian Heidelbach, Detlef Krauße, Ingrid
304 Blanchard, and Vera Laurenz-Heuser for SEM and EPMA assistance, and Eleanor Jennings
305 for microprobe standard synthesis. We are grateful to Antonio Acosta-Vigil and two
306 anonymous reviewers for their helpful and constructive comments. This work was supported
307 by a grant (STE1105/12-1) from the German Research Foundation (Deutsche
308 Forschungsgemeinschaft, DFG) within the Priority Program "Building a Habitable Earth"
309 (SPP 1833). A.M.R. was funded by a research assistantship from the College of
310 Environmental and Life Sciences at the University of Rhode Island during the writing of this
311 manuscript.
312

313 **REFERENCES CITED**

314 Anento, N., Serra, A., and Osetsky, Y. (2017) Effect of nickel on point defects diffusion in
315 Fe-Ni alloys. Acta Materialia, 132(15): 367–373.
316 Blanchard, I., Jennings, E., Franchi, I.A., Zhao, X., Petitgirard, S., Miyajima, N., Jacobson,
317 S., and Rubie, D. (2019) The fact of carbon during Earth's core-mantle
318 differentiation. EarthArXiv. doi:10.31223/osf.io/9t7ps
319 Campbell, F.C. (2008) Elements of Metallurgy and Engineering Alloys, 671 p. ASM
320 International, Materials Park, Ohio.

Dasgupta, R., Chi, N., Shimizu, N., Buono, A.S., and Walker, D. (2013) Carbon solution and partitioning between metallic and silicate melts in a shallow magma ocean: implications for the origin and distribution of terrestrial carbon. Geochimica et Cosmochimica Acta, 102, 191–212.

Dobson, D.P., and Wiedenbeck, M. (2002) Fe- and C-self-diffusion in liquid Fe_3C to 15 GPa. Geophysical Research Letters, 29(21), doi:10.1029/2002GL015536.

Fischer, R.A., Cottrell, E., Hauri, E., Lee, K.K.M., and Le Voyer, M. (2020) The carbon content of Earth and its core. Proceedings of the National Academy of Sciences, doi:10.1073/pnas.1919930117

Goldschmidt, H.J. (1967) Interstitial Alloys, 643 p. Springer, Boston.

Hazen, R.M., and Schiffries, C.M. (2013) Why deep carbon? Reviews in Mineralogy and Geochemistry, 75, 1–6.

Ni, H., Hui, H., and Steinle-Neumann, G. (2015) Transport properties of silicate melts. Reviews of Geophysics, 53(3), 715–744.

Ichikawa, H., and Tsuchiya, T (2015) Atomic transport property of Fe-O liquid alloys in the Earth's outer core P,T condition. Physics and Earth and Planetary Interiors, 247, 27–35.

Li, Y., Dasgupta, R., and Tsuno, K. (2014) The effects of sulfur, silicon, water, and oxygen fugacity on carbon solubility and partitioning in Fe-rich alloy and silicate melt systems at 3 GPa and 1600°C: Implications for core–mantle differentiation and degassing of magma oceans and reduced planetary mantles. Earth and Planetary Science Letters, 415, 54–66.

Li, Y., Dasgupta, R., Tsuno, K., Monteleone, B., and Shimizu, N. (2016) Carbon and sulfur budget of the silicate Earth explained by accretion of differentiated planetary embryos. Nature Geoscience, 9, 781–785.

346 Ohmura, S., Tsuchiya, T., and Shimojo, F. (2020) Structures of liquid iron–light-element
347 mixtures under high pressure. Physica Status Solidi B, doi:10.1002/pssb.202000098
348 Okamoto, H. (1992) The C-Fe (carbon-iron) system. Phase Equilibria, 13(5), 543–565.
349 Osetsky, Y., Anento, N., and Serra, A., and Terentyev, D. (2015) The role of nickel in
350 radiation damage of ferritic alloys. Acta Materialia, 84, 368–374.
351 Poirier J.P. (1988) Transport properties of liquid metals and viscosity of the Earth's core.
352 Geophysical Journal International, 92, 99–105.
353 Posner, E.S., Rubie, D.C., Frost, D.J., Vlček, V., and Steinle-Neumann, G. (2017a) High P-T
354 experiments and first principles calculations of the diffusion of Si and Cr in liquid
355 iron. Geochimica et Cosmochimica Acta, 203, 323–342.
356 Posner, E.S., Rubie, D.C., Frost, D.J., and Steinle-Neumann, G. (2017b) Experimental
357 determination of oxygen diffusion in liquid iron at high pressure. Earth and Planetary
358 Science Letters, 464, 116–123.
359 Posner, E.S., Steinle-Neumann, G., Vlček, V., and Rubie, D.C. (2017c) Structural changes
360 and anomalous self-diffusion of oxygen in liquid iron at high pressure. Geophysical
361 Research Letters, 44, 3526–3534.
362 Posner, E.S., Schmickler, B., and Rubie, D.C. (2018) Self-diffusion and chemical diffusion in
363 peridotite melt at high pressure and implications for magma ocean viscosities.
364 Chemical Geology, 502, 66–75.
365 Posner, E.S., and Steinle-Neumann, G. (2019) Mass transport and structural properties of
366 binary liquid iron alloys at high pressure. Geochemistry, Geophysics, Geosystems, 20,
367 3556–3568.
368 Press, W.H., Teulolsky, S.A., Vetterling, W.T., and Flannery, B.P. (2002) Numerical recipes
369 in C++, 2nd ed., 1002 p. Cambridge University Press, Cambridge.

Rubie, D.C. (1999) Characterising the sample environment in multianvil high-pressure experiments. Phase Transitions, 68, 431–451.

Rubie, D.C., Melosh, H.J., Reid, J.E., Liebske, C., and Righter, K. (2003) Mechanisms of metal–silicate equilibration in the terrestrial magma ocean. Earth and Planetary Science Letters, 205, 239–255.

Rubie, D.C., Nimmo, F., and Melosh, H.J. (2015) Formation of the Earth's Core. In: Gerald Schubert (Ed.) Treatise on Geophysics Vol. 9: Evolution of the Earth, 2nd edition, Oxford: Elsevier. pp. 43–79.

Sanloup, C., Guyot, F., Gillet, P., Fiquet, G., Hemley, R.J., Mezouar, M., and Martinez, I. (2000) Structural changes in liquid Fe at high pressures and temperatures from synchrotron X-ray diffraction. Europhysics Letters, 52, 151–157.

Sobolev, A., and Mirzoev, A. (2013) Ab initio studies of the short-range atomic structure of liquid iron-carbon alloys. Journal of Molecular Liquids, 179, 12–17.

Swartzendruber, L.J. (1982) The Fe (iron) system. Bulletin of Alloy Phase Diagrams, 3(2), 161–165.

Terasaki, H., Nishida, K., Shibazaki, Y., Sakamaki, T., Suzuki, A., Ohtani, E., and Kikegawa, T. (2010) Density measurement of Fe_3C liquid using X-ray absorption image up to 10 GPa and effect of light elements on compressibility of liquid iron. Journal of Geophysical Research, 115, B06207.

Umemoto, K., and Hirose, K. (2015) Liquid iron-hydrogen alloys at outer core conditions by first-principles calculations. Geophysical Research Letters, 42, 7513–7520.

Wang, J., Chen, B., Williams, Q., and Manghnani, M.H. (2019) Short- and intermediate-range structure and dynamics of Fe-Ni-C liquid under compression. Frontiers in Earth Science, 7, 258.

Wood, I.G., Vočadlo, L., Knight, K.S., Dobson, D.P., Marshall, G., Price, D., and Brodholt, J. (2004) Thermal expansion and crystal structure of cementite, Fe3C, between 4 and 600 K determined by time-of-flight neutron powder diffraction. Journal of Applied Crystallography, 37, 82–90.

Yang, L., Simnad, M.T., and Derge, G. (1956) Self-diffusion of iron in molten Fe-C alloys. JOM, 8, 1577–1580.

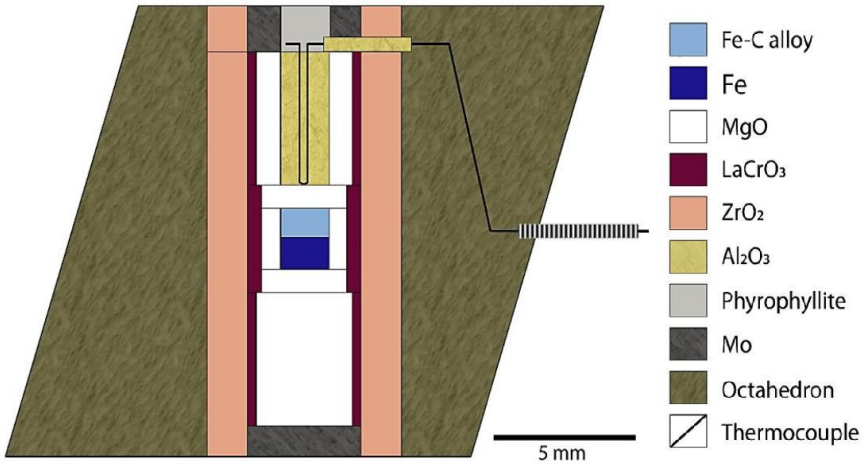

Fig. 1: Schematic diagram of the multi-anvil experimental setup. The diffusion couple is held vertically in the MgO capsule with the alloy on top to maintain gravitational stability.

This is the peer-reviewed, final accepted version for American Mineralogist, published by the Mineralogical Society of America.
The published version is subject to change. Cite as Authors (Year) Title. American Mineralogist, in press.
DOI: https://doi.org/10.2138/am-2021-7644. http://www.minsocam.org/

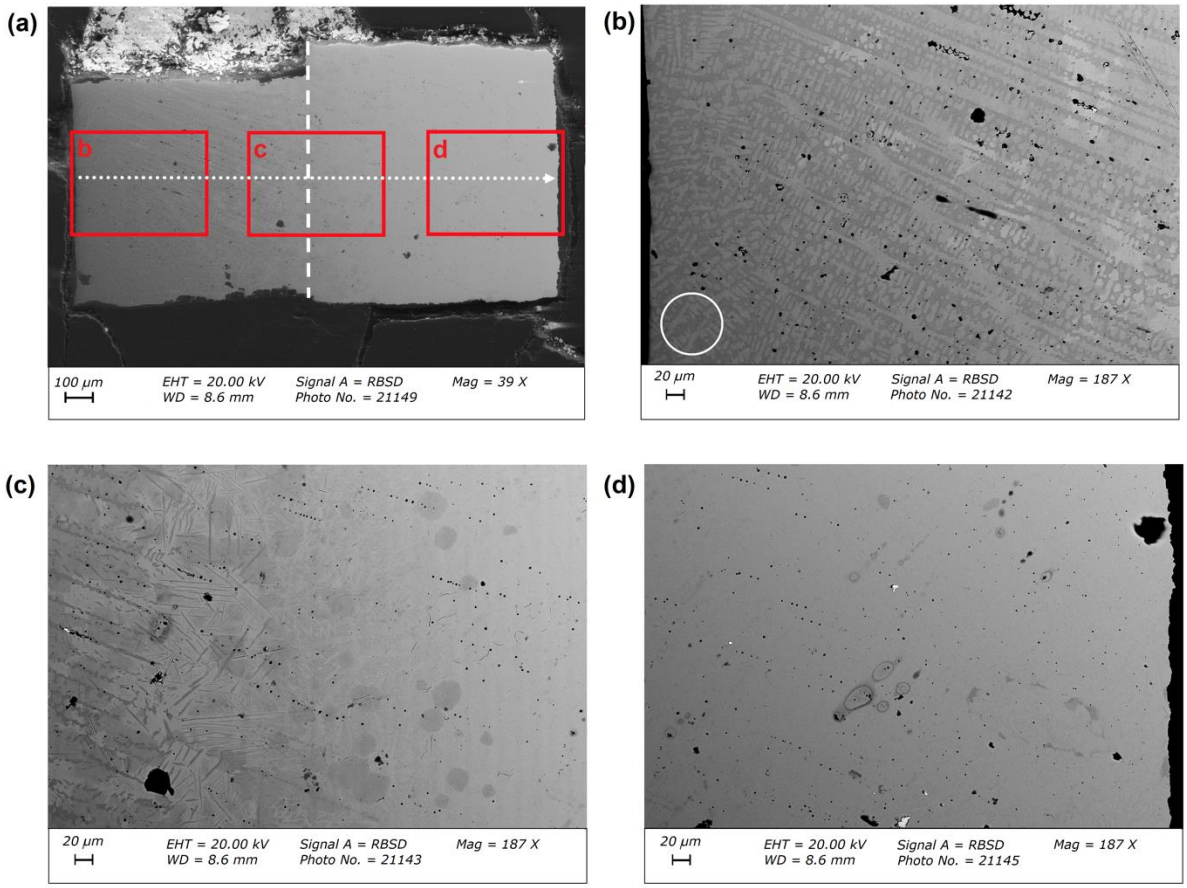

Fig. 2: Backscattered electron images of the quenched sample of expt. #303 performed at 3 GPa (Table 1). (a) Fe and C concentration profiles were measured along a transect from one end of the sample to the other (white dotted horizontal line) on a line perpendicular to the diffusion couple interface (white dashed vertical line). The labeled red boxes show the locations of high-magnification images of the initially (b) carbon-rich and (d) carbon-free sides of the diffusion couple and (c) the interface region. A dendritic quench texture of

intergrown high-carbon (dark gray) and low-carbon (light gray) phases is pervasive in (b) and the left side of (c), whereas the right side of (c) and (d) show a more uniform low-carbon texture. A relatively large beam diameter of ~70 μm, e.g., white circle in (b), was thus used to effectively analyze both phases. The carbon concentration profile of this sample is shown in the top-left panel of Fig. 4a.

This is the peer-reviewed, final accepted version for American Mineralogist, published by the Mineralogical Society of America.
The published version is subject to change. Cite as Authors (Year) Title. American Mineralogist, in press.
DOI: https://doi.org/10.2138/am-2021-7644. http://www.minsocam.org/

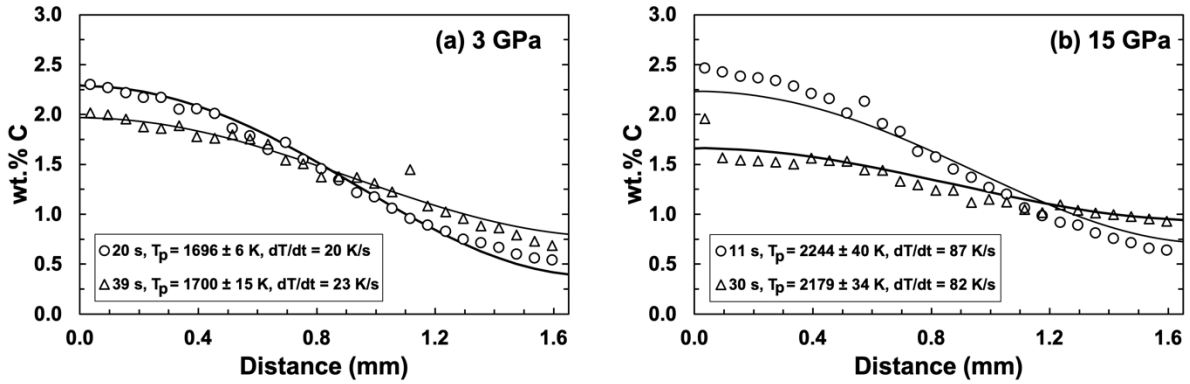

Fig. 3: Carbon concentration profiles measured from two experiments each conducted at (a) 3 GPa and ~1700 K and (b) 15 GPa and ~2210 K, in each case with similar annealing temperatures (T_p) and heating rates (dT/dt), but different durations at T_p (t_p). The model fits to the data (solid curves) represent a global solution to all experiments conducted at (a) 3 GPa (N = 5) and (b) 15 GPa (N = 5), as shown in Fig. 4. Peak anneal temperature was more readily reproduced in the low-P experiment due to the slower heating rate (Table 1).

This is the peer-reviewed, final accepted version for American Mineralogist, published by the Mineralogical Society of America.
The published version is subject to change. Cite as Authors (Year) Title. American Mineralogist, in press.
DOI: https://doi.org/10.2138/am-2021-7644. http://www.minsocam.org/

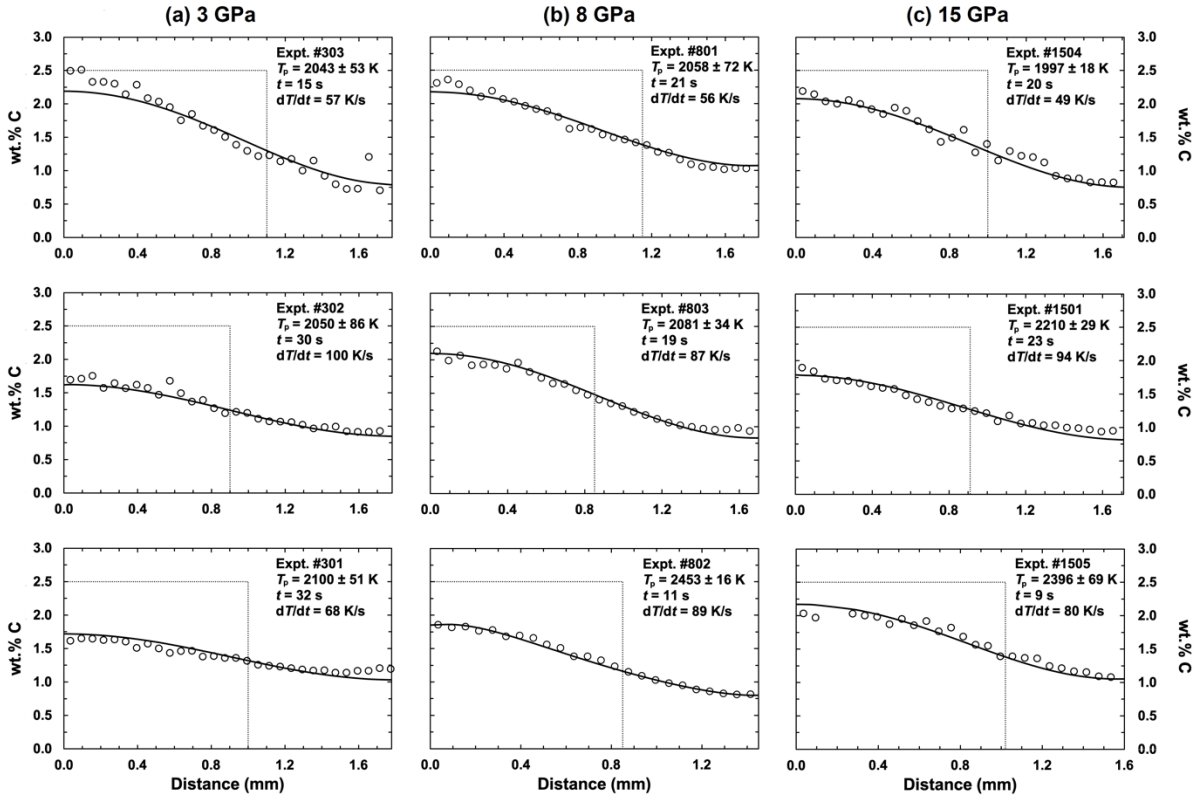

Fig. 4: Carbon concentration profiles for experiments conducted at (a) 3 GPa, (b) 8 GPa, and (c) 15 GPa (Table 1). Dashed lines show the optimized interface locations and model initial carbon profiles. The model fits to the data (solid curves) represent the simultaneous global solution to all experiments at each pressure; N = 5 at 3 and 15 GPa (the other two fitted profiles are shown in Figs. 3a and 3b, respectively) and N = 3 at 8 GPa. Some model curves show a greater misfit with respect to the experimental data owing to the simultaneous fitting of all profiles at a given pressure, which is required to account for non-isothermal diffusion during heating (see Posner et al., 2017a).

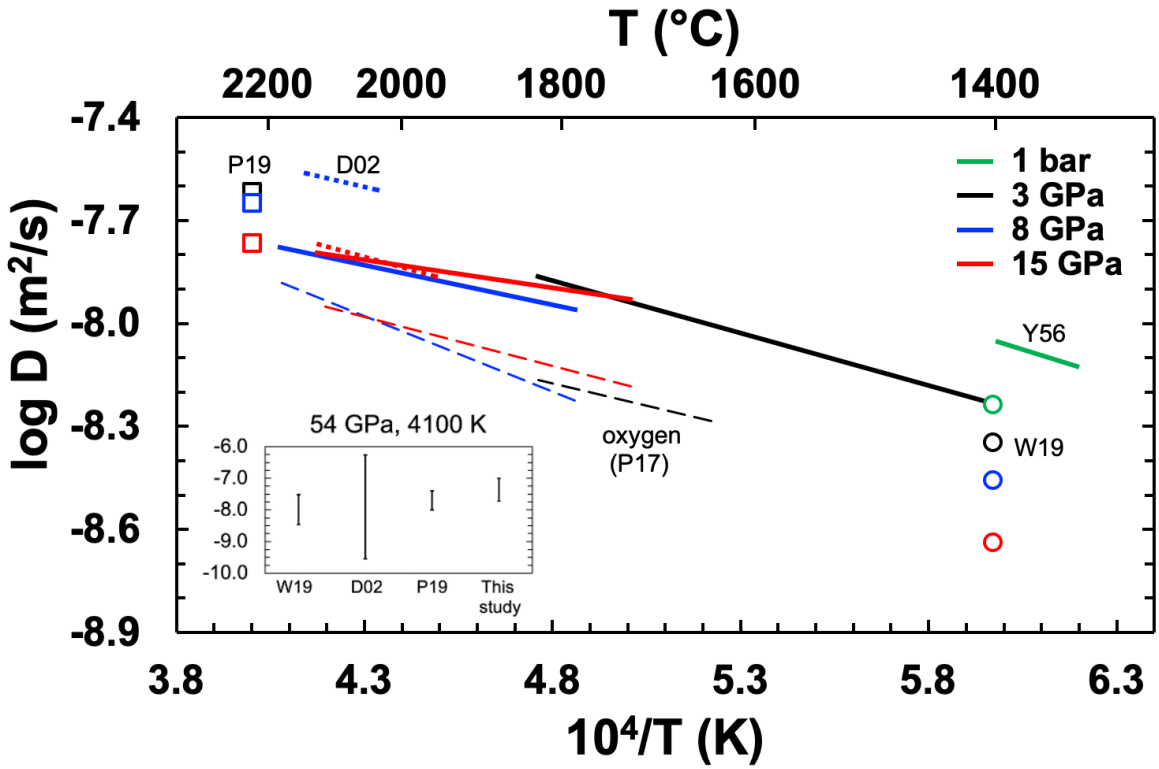

Fig. 5: Arrhenius plot for carbon chemical diffusion in liquid iron measured in this study, represented as solid curves at 3 GPa (black), 8 GPa (blue), and 15 GPa (red), alongside carbon self-diffusion data in liquid Fe_3C by Dobson and Wiedenbeck (2002) (D02, dotted curves) over smaller *T* ranges at 8 and 15 GPa, ambient-*P* data for Fe-2.5wt.%C by Yang et al. (1956) (Y56, green solid curve), and oxygen diffusion in liquid Fe using parameters determined by high *P*-*T* experiments by Posner et al. (2017b) (P17, dashed curves). Squares and circles represent DFT-MD results of carbon self-diffusion in liquid $Fe_{0.96}C_{0.04}$ by Posner and Steinle-Neumann (2019) (P19) at 2500 K and in liquid $Fe_{0.73}Ni_{0.07}C_{0.20}$ by Wang et al. (2019) (W19) at 1675 K, respectively. The inset compares diffusion coefficients extrapolated to *P*-*T* conditions relevant to core formation in a deep magma ocean (54 GPa, 4100 K; Rubie et al., 2015). Extrapolation of the W19 results was estimated by varying ΔE in the range of 30–60 $kJ \cdot mol^{-1}$; diffusivity of P19 was obtained by interpolating between available *P*-*T* points.

466

Table 1: Experimental conditions and isobaric Arrhenius parameters, D_0^* and ΔH^*, refined from the least-squares best-fit to all concentration profiles measured at each pressure. Errors are only assigned to ΔH^* owing to the correlated nature of D_0^* and ΔH^*, as discussed in Posner et al. (2017a).

P	Expt. #	Peak T ($T_p \pm 1\sigma$)	Heating rate (dT/dt)	Time at T_p (t_P)	D_0^*	ΔH^*	χ^2_{red}
(GPa)		(K)	($K \cdot s^{-1}$)	(s)	(10^{-7} $m^2 \cdot s^{-1}$)	($kJ \cdot mol^{-1}$)	
3	311	1696 ± 6	20	39	3.9	59 ± 5	0.9544
3	312	1700 ± 15	23	20			
3	303	2043 ± 53	57	15			
3	302	2050 ± 86	100	30			
3	301	2100 ± 51	68	32			
8	801	2058 ± 72	56	21	1.4	44 ± 4	0.3960
8	803	2081 ± 34	87	19			
8	802	2454 ± 16	89	11			
15	1504	1997 ± 18	49	20	0.77	31 ± 9	0.9254
15	1511	2179 ± 34	82	30			
15	1501	2210 ± 29	94	23			
15	1512	2244 ± 40	87	11			
15	1505	2396 ± 69	80	9			

467
468
469

Table 2: Comparison of refined Arrhenian parameters for solute diffusion in liquid iron at high pressure, according to Eq. (1). All ΔE values are consistent (<70 kJ mol^{-1}), whereas reported ΔV vary over a considerably wider range. References are: DW02, Dobson and Wiedenbeck (2002); W19, Wang et al. (2019); P17a, Posner et al. (2017a); P17b, Posner et al. (2017b); UH15, Umemoto and Hirose (2015).

P **(GPa)**	***T*** **(K)**	**Diffusing element**	D_0 (10^{-7} $m^2 \cdot s^{-1}$)	ΔE (kJ mol^{-1})	ΔV (10^{-6} $m^3 \cdot mol^{-1}$)	**Technique**	**Reference**
8–15	2228–2413	C	2.9 ± 2.1	37 ± 3	1.3 ± 0.5	Isotopic tracer[a]	DW02
0.3–67	1673		–	–	1.2 ± 0.3[c] 0.61 ± 0.09[d]	Self-diffusion[b]	W19
3–15	1700–2450		1.4 ± 0.5	43 ± 6	−0.06 ± 0.19	Chemical diffusion[a]	This study
1–18	1873–2428	Si	0.57 ± 0.13	40 ± 4	0.41 ± 0.06	Chemical diffusion[a]	P17a
		Cr	0.66 ± 0.27	46 ± 7	0.34 ± 0.11		
3–18	1975–2673	O	2.7 ± 1.0	62 ± 6	0.11 ± 0.11	Chemical diffusion[a]	P17b
~100–350	4000–7000	H	8.82[e] 6.41[f] 5.07[g]	67 55 48	0.20 0.18 0.13	Self-diffusion[b]	UH15

[a] Multi-anvil experiments; [b] MD simulation; [c] $\lesssim$ 5 GPa; [d] $\gtrsim$ 5 GPa; [e] $Fe_{100}H_{28}$; [f] $Fe_{88}H_{40}$; [g] $Fe_{76}H_{52}$

470